The Astrophysical Journal Letters, 999:L16 (8pp), 2026 March 1 https://doi.org/10.3847/2041-8213/ae4104
© 2026. The Author(s). Published by the American Astronomical Society.
OPEN ACCESS

# $^{56}$Ni Production in Long-lived Binary Neutron Star Merger Remnants

Maximilian Jacobi[1], Fabio Magistrelli[1], Eleonora Loffredo[2], Giacomo Ricigliano[3,4], Leonardo Chiesa[5,6], Sebastiano Bernuzzi[1], Albino Perego[5,6], and Almudena Arcones[3,4,7]
[1] Theoretisch-Physikalisches Institut, Friedrich-Schiller-Universität Jena, 07743, Jena, Germany; maximilian.jacobi@uni-jena.de
[2] INAF—Osservatorio Astronomico d'Abruzzo, Via M. Maggini snc, 64100 Teramo, Italy
[3] Max-Planck-Institut für Kernphysik, Saupfercheckweg 1, Heidelberg 69117, Germany
[4] Institut für Kernphysik, Technische Universität Darmstadt, Schlossgartenstr. 2, Darmstadt 64289, Germany
[5] Dipartimento di Fisica, Universitá di Trento, Via Sommarive 14, 38123 Trento, Italy
[6] INFN-TIFPA, Trento Institute for Fundamental Physics and Applications, via Sommarive 14, I-38123 Trento, Italy
[7] GSI Helmholtzzentrum für Schwerionenforschung GmbH, Planckstr. 1, Darmstadt 64291, Germany
*Received 2025 November 4; revised 2026 January 28; accepted 2026 February 1; published 2026 February 26*

## Abstract

We investigate the nucleosynthesis and kilonova emission based on numerical-relativity binary neutron star merger simulations that incorporate a two-moment neutrino-transport scheme. Unlike in previous works with simpler neutrino treatments, a massive, fast (up to $v = 0.3c$), proton-rich neutrino-driven wind develops in the postmerger phase of the simulations as long as the merger remnant does not collapse to a black hole. We evolve the ejecta for 100 days after the merger using 2D ray-by-ray radiation-hydrodynamics simulations coupled in situ to a complete nuclear network. The most abundant nucleosynthesis products are He, $^{56}$Ni, and $^{56}$Co. We find a total yield of $\sim 10^{-3} M_{\odot}$ of $^{56}$Ni for all mergers that produce massive neutron star remnants, independently of the mass ratio and equations of state. After a few days, the decay of $^{56}$Ni and later $^{56}$Co becomes the primary source of heating in the matter expanding above the remnant. As a result, the kilonova light curve flattens on timescales of days for polar observation angles. This is an important effect that should be included in future models of kilonova light curves. Furthermore, the observation of a $^{56}$Ni–$^{56}$Co feature could serve as a clear indicator for the presence of a long-lived neutron star remnant in future kilonova observations.

*Unified Astronomy Thesaurus concepts:* Explosive nucleosynthesis (503); Neutron stars (1108)

## 1. Introduction

The mergers of binary neutron star (BNS) systems produce hot and dense ejecta, in which heavy elements are synthesized by the *r*-process (E. Symbalisty & D. N. Schramm 1982; D. Eichler et al. 1989; C. Freiburghaus et al. 1999). During the expansion of the ejecta, heat generated by the radioactive decay of the newly formed heavy elements powers a fast transient, the kilonovae (KNs; L.-X. Li & B. Paczynski 1998; B. D. Metzger et al. 2010). The combined heating of many *r*-process nuclei decaying simultaneously typically leads to a power law–like heating rate $\propto t^{-\alpha}$ with $\alpha \approx 1.1$–$1.4$ (see, e.g., B. D. Metzger et al. 2010; O. Korobkin et al. 2012). Investigations of the KN AT2017gfo found a good agreement of the light curve with radioactive heating from *r*-process nuclei (M. Tanaka et al. 2017; E. Waxman et al. 2018; P. S. Cowperthwaite et al. 2017; M. M. Kasliwal et al. 2017; A. Murguia-Berthier et al. 2017; M.-R. Wu et al. 2019). This is broadly consistent with simulations that find dynamical ejecta are typically at least mildly neutron rich (S. Rosswog et al. 1999; K. Hotokezaka et al. 2013; D. Radice et al. 2018; V. Nedora et al. 2021; K. Kiuchi et al. 2023), although the ejected mass is insufficient to explain the luminosity and no ab initio simulation can yet quantitatively reproduce the light curves.

Tens to hundreds of milliseconds after the merger, spiral-wave (V. Nedora et al. 2019, 2021) and neutrino-driven winds (L. Dessart et al. 2009; A. Perego et al. 2014; D. Martin et al. 2015; S. Fujibayashi et al. 2020) can launch $\gtrsim 10^{-3} M_{\odot}$ of ejecta from the remnant accretion disk as long as the remnant does not collapse to a black hole (BH) shortly after the merger. Recent long-term BNS merger simulations presented in O. Just et al. (2023), D. Radice & S. Bernuzzi (2023), F. Schianchi et al. (2024), S. Bernuzzi et al. (2025), and A. Neuweiler et al. (2025) have found that a large fraction of the neutrino-driven wind exhibits electron fractions close to 0.5. These simulations employ a two-moment "M1" neutrino-transport scheme, unlike previous long-time simulations of BNS mergers, which typically use a more approximate leakage-based neutrino transport (V. Nedora et al. 2021; L. Combi & D. M. Siegel 2023; K. Kiuchi et al. 2023). As a consequence of the relatively high electron fraction, the nucleosynthesis in the neutrino-driven wind is dominated by an $\alpha$-rich freeze-out and by the production of $^{56}$Ni. In contrast to *r*-process powered transients, the heating rate in the proton-rich wind ejecta follows the exponential decay of $^{56}$Ni and $^{56}$Co with half-lives of 6 and 77 days, respectively. If a large enough amount of $^{56}$Ni is produced in the neutrino-driven ejecta from BNS mergers, this could observably alter the associated KN light curve compared to what would be expected from purely neutron-rich ejecta. O. Just et al. (2023) find that iron-group elements are produced in the neutrino-driven wind. However, they do not report a significant enhancement of the KN luminosity. While it was confirmed that the decay of $^{56}$Ni alone cannot account for the transient observed in 2017 (P. S. Cowperthwaite et al. 2017), to our knowledge it has not been investigated whether the combined heating from $^{56}$Ni and *r*-process elements are compatible with AT2017gfo.

In this work, we investigate the production of $^{56}$Ni in neutrino-driven ejecta from BNS mergers and the impact on the KN emission based on the simulations presented in

Original content from this work may be used under the terms of the Creative Commons Attribution 4.0 licence. Any further distribution of this work must maintain attribution to the author(s) and the title of the work, journal citation and DOI.

**Table 1**
Overview of the BNS Models Considered in This Work

| Model | $M_1$ ($M_\odot$) | $M_2$ ($M_\odot$) | $t_{\rm pm}$ (ms) | $t_{\rm BH}$ (ms) | $M_{\rm ej}$ ($10^{-3}M_\odot$) | $M_{\rm ej}^{n}$ ($10^{-3}M_\odot$) | $M_{\rm ej}^{p}$ ($10^{-3}M_\odot$) | $M_{\rm ej}^{\rm He}$ ($10^{-3}M_\odot$) | $M_{\rm ej}^{\rm Ni}$ ($10^{-3}M_\odot$) |
|---|---|---|---|---|---|---|---|---|---|
| BLh_q1.49 | 1.64 | 1.15 | 103 | 114 | 10.85 | 4.01 | 3.72 | 3.03 | 0.84 |
| DD2_q1.77 | 1.81 | 1.08 | 111 | >130 | 25.31 | 19.30 | 1.59 | 1.56 | 0.43 |
| DD2_q1.0 | 1.35 | 1.35 | 79 | >79 | 5.80 | 1.18 | 1.53 | 1.23 | 0.41 |
| SFHo_q1.0 | 1.35 | 1.35 | 35 | 8.3 | 6.25 | 3.51 | 0.00 | 0.09 | 0.01 |

**Note.** Given are initial gravitational BNS masses $M_1$ and $M_2$, the simulated postmerger time $t_{\rm pm}$, the time until BH formation $t_{\rm BH}$, the total ejecta mass $M_{\rm ej}$, the mass of very neutron-rich ($Y_e < 0.25$) ejecta $M_{\rm ej}^{n}$, and proton-rich ($Y_e > 0.5$) ejecta $M_{\rm ej}^{p}$ and the total mass of ejected He and $^{56}$Ni $M_{\rm ej}^{\rm He}$, $M_{\rm ej}^{\rm Ni}$, respectively. Ejecta masses are inferred using the Bernoulli criterion ($-hu_t > 1$).

D. Radice & S. Bernuzzi (2023), E. M. Gutiérrez et al. (2025), and S. Bernuzzi et al. (2025).

## 2. Methods

We analyze and compare the ejection of proton-rich material in four numerical relativity (NR) BNS merger simulations summarized in Table 1.

They consist of two asymmetric ($q > 1$), BLh_q1.49 and DD2_q1.77; and two symmetric ($q = 1$) BNS systems, SFHo_q1.0 and DD2_q1.0, employing three different microphysical equations of states (EOSs): SFHo (A. W. Steiner et al. 2013), DD2 (S. Typel et al. 2010; M. Hempel & J. Schaffner-Bielich 2010), and BLh (I. Bombaci & D. Logoteta 2018; D. Logoteta et al. 2021). All models discussed in this work have been presented in previous publications (D. Radice & S. Bernuzzi 2023; S. Bernuzzi et al. 2025; E. M. Gutiérrez et al. 2025). Note that we use the baryon-mass ratio $q = M_1^{\rm b}/M_2^{\rm b} \geqslant 1$ for the naming of models to stay consistent with the naming convention in S. Bernuzzi et al. (2025), while Table 1 lists the gravitational masses $M_1$, $M_2$.

All simulations are performed with the THC code (D. Radice & L. Rezzolla 2012; D. Radice et al. 2014a, 2014b, 2015, 2016, 2022), which is built on top of the Cactus framework (T. Goodale et al. 2003; E. Schnetter et al. 2007). The simulations employ a truncated, two-moment gray neutrino-transport scheme that retains all nonlinear neutrino-matter coupling terms (D. Radice et al. 2022) and uses the Minerbo closure. The set of weak reactions included in the transport scheme is described in e.g., F. Galeazzi et al. (2013), D. Radice et al. (2016), and A. Perego et al. (2019). The general-relativistic hydrodynamics equations are formulated in conservative form (see D. Radice et al. 2018 for details on the precise equations solved here) and augmented by a large-eddy scheme that accounts for angular momentum transport due to magnetohydrodynamical effects (D. Radice 2017, 2020; D. Radice & S. Bernuzzi 2023).

The equal-mass simulations, DD2_q1.0 and SFHo_q1.0, consist of two $1.35M_\odot$ neutron stars (NSs). In the BLh_q1.49 model, the BNS masses are compatible with the chirp mass measured in GW170817, and the mass ratio lies at the upper bound of the constraints inferred with low spin priors (B. P. Abbott et al. 2019). The DD2_q1.77 model exhibits an even larger mass ratio and as such, represents a comparably extreme case. Of the four binaries considered in this work, only the remnant in SFHo_q1.0 collapses to a BH in the gravitational-wave driven phase, while the central remnant is a massive NS for the duration of the simulation in the other three models. These models eject matter for the full duration of the simulations until ∼100 ms post merger.

After the time at which the ejecta analyzed in this work were extracted, we continued the simulation of the models BLh_q1.49 and DD2_q1.77. In BLh_q1.49, the merger remnant collapses after 114 ms postmerger (i.e., shortly after the time at which the analysis in this Letter is performed). The simulation of DD2_q1.77 was performed until ∼130 ms post merger without the remnant collapsing to a BH. At this point, the evolution of the gauge becomes unstable, and the simulation crashes. The model DD2_q1.0 is studied in many works in the literature, including S. Fujibayashi et al. (2020), who evolved the postmerger remnant in axisymmetry for several seconds without it collapsing. We do not expect that further evolving this model will result in a qualitative change of the ejecta properties unless it is evolved to viscous timescales, which is not computationally feasible with our 3D M1 GRMHD simulations. The ejection of matter stops shortly after collapse in the model SFHo_q1.0, so we do not continue the simulation further.

We evolve the ejecta and the nucleosynthesis during the expansion up to $t = 100$ days with the Lagrangian radiation-hydrodynamics code SNEC (V. Morozova et al. 2015; Z. Wu et al. 2022) coupled to the SkyNet nuclear network (J. Lippuner & L. F. Roberts 2017), as described in F. Magistrelli et al. (2024, 2025).

Ejecta properties are recorded on the extraction sphere as a function of time and the azimuthal and polar angles. The data are then averaged over the azimuthal angle, weighted by the density as described in F. Magistrelli et al. (2024). Finally, we create initial Lagrangian profiles for SNEC with the layered shell-by-shell method described in Z. Wu et al. (2022). The dependency on the polar angle of the ejecta properties is approximately included in a ray-by-ray fashion by mapping the initial profile into an effective 1D problem for a number of angular bins. One full simulation includes 26 rays uniformly spaced in the polar angle, ranging from $\theta = 0$ (polar) to $\theta = \pi/2$ (equatorial), assuming mirror symmetry across the equatorial plane. To ensure that all the intensive quantities (including the density) remain unaltered, we multiply the total mass by the scaling factor $\lambda_\theta = 4\pi/\Delta\Omega$, where $\Delta\Omega \simeq 2\pi \sin\theta\, d\theta$ is the solid angle of the angular bin. Each angular section is discretized radially into 1000 fluid elements and evolved independently up to $t = 100$ days. Nonradial fluid motion is neglected in this approach, which we expect to slightly change the angular distribution of the ejecta and therefore, the observer-angle dependence of the

light curve. However, this effect is most likely negligible compared to uncertainties in the EOSs and the numerical simulations.

We note that the ejecta velocities change by up to a few percent of the speed of light after the transition from the THC to the SNEC simulations. This is likely caused by the method of initialization of the SNEC simulations (see Z. Wu et al. 2022), the transition from a general relativistic to a Newtonian description of gravity, and the switch of the employed EOSs. Because the regions that constitute $^{56}$Ni are unaffected, the conclusions of this Letter remain unchanged.

The nuclear network includes 7836 isotopes up to $^{337}$Cn and uses the JINA REACLIB (R. H. Cyburt et al. 2010) and the same setup as in J. Lippuner & L. F. Roberts (2015) and A. Perego et al. (2022). We self-consistently couple the effects of nuclear heating from the in situ network with the hydrodynamics evolution. The thermalization of energy produced by nuclear reactions is treated explicitly for contributions from $\gamma$-rays, $\alpha$ particles, electrons, and other nuclear reactions products and is described in detail in F. Magistrelli et al. (2024). For some ejecta components, the temperature at the moment of mapping has already dropped below $\sim$6 GK. To ensure consistent initialization in nuclear statistical equilibrium (NSE) conditions, we extrapolate to earlier times using an analytic trajectory starting at $T = 8$ GK as described in F. Magistrelli et al. (2025). The details of the extrapolation change the $^{56}$Ni abundance by $\sim$10% (see Appendix B in F. Magistrelli et al. 2025). To calculate the luminosity in each angular section, we employ the analytic, time-independent opacity described in Z. Wu et al. (2022). We note that F. Magistrelli et al. (2025) investigate the impact of composition and time-dependent opacities and find that the overall shape of the light curve is impacted. The KN light curves are combined depending on the viewing angle as described in D. Martin et al. (2015) and A. Perego et al. (2017) to approximately take nonradial photon motion into account. Note that this recombination assumes spherical symmetry, which, given the asymmetry of the optical depth in the ejecta, might not be fully accurate. Despite these approximations, we do not expect the conclusions drawn in this Letter to be affected.

KN spectra from each angular section are computed using the radiative transfer spectral synthesis code TARDIS (W. E. Kerzendorf & S. A. Sim 2014). The density, velocity, and composition profiles are obtained by rebinning the fluid elements outside the photosphere into 50 radial shells, while the input luminosity is given by the bolometric luminosity, $L = \sum_\theta L_\theta / \lambda_\theta$, where $L_\theta$ is the luminosity from the individual ray. We use the atomic dataset developed by J. H. Gillanders et al. (2022), considering atomic lines of elements with $Z \leqslant 40$ (the first nine rows in Table 1 of J. H. Gillanders et al. 2022). Since we are mostly interested in modeling the polar ejecta, which predominantly synthesize light $r$-process elements, this limited line list is likely sufficient. Ionization and excitation are treated with the local thermal equilibrium and dilute local thermal equilibrium approximations, respectively, while the "macroatom" scheme is employed for line interaction treatment. In addition to KN spectra obtained from each ray, we combine them for the fixed viewing angle, following the same weighting prescription used for the luminosity computed in the SNEC simulations.

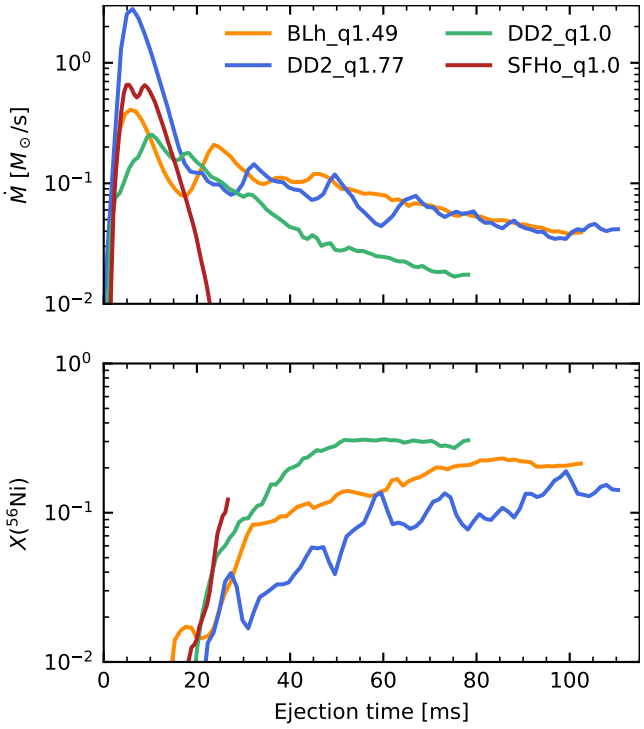



**Figure 1.** Top panel: mass-ejection rate for the considered BNS models. Bottom panel: $^{56}$Ni mass fraction that the fluid elements will achieve after 10 s as a function of their ejection time. The $x$-axis shows the time of ejection defined as the time at which the fluid elements cross the sphere at $\sim$450 km.

## 3. Results

### 3.1. Ejecta Distribution and Properties

The upper panel of Figure 1 shows the mass-ejection rate as a function of ejection time for the four models considered in this work. Here "ejection time" refers to the time at which the Lagrangian fluid elements cross the sphere at $\sim$450 km and is therefore slightly delayed with respect to the actual time of ejection from the merger remnant. All models exhibit dynamical ejecta of tidal and shock-heated origin within the first 10 ms after merger. After that, oscillations of the massive NS drive a spiral-wave wind that ejects moderately neutron-rich matter, leading to an oscillatory mass-ejection rate. This ejection continues until the end of the simulation or the collapse of the remnant. Such a spiral-wave wind is stronger in the asymmetric models, especially in DD2_q1.77, where it persists until the end of the simulation.

The neutrino-driven mass ejection starts $\sim$10 ms after the merger in the polar direction ($\theta \lesssim 30^\circ$) and continues until the end of the simulation or the collapse of the remnant. In the almost exclusively proton-rich polar ejecta, the freeze-out from NSE is dominated by $\alpha$ particles, resulting in a final He mass fraction of $\sim$10%, in agreement with the values found in O. Just et al. (2023). This could lead to a detectable feature in the KN spectrum after a few days (A. Perego et al. 2022; Y. Tarumi et al. 2023; A. Sneppen et al. 2024a), indicating the presence of a long-lived NS remnant (A. Sneppen et al. 2024b).

Furthermore, $\alpha$ captures synthesize nuclei along the $Z = N$ line on the nuclear chart ending at $^{56}$Ni due to its doubly magic nature. The lower panel of Figure 1 shows the $^{56}$Ni mass fraction of the fluid elements as a function of the time at which they cross the extraction sphere. The $^{56}$Ni fraction $X(^{56}\mathrm{Ni})$

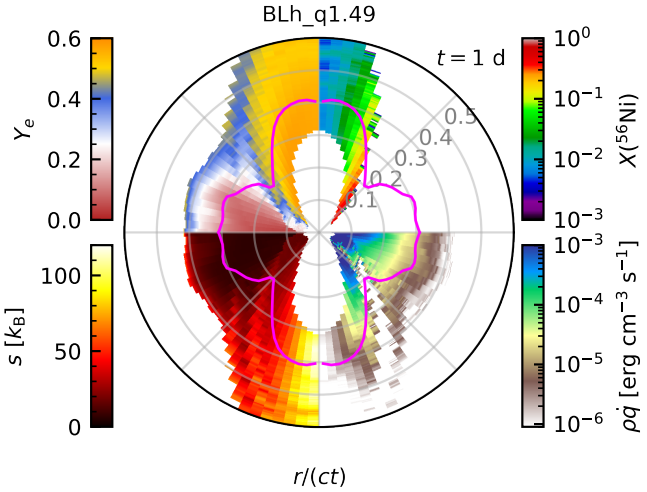



**Figure 2.** Spatial distribution of the ejecta of the BLh_q1.49 model after 1 day. Top-left quadrant: electron fraction at the beginning of the SNEC simulation. Top-right quadrant: mass fraction of $^{56}$Ni. Bottom-left quadrant: initial entropy at the beginning of the SNEC simulation. Bottom-right quadrant: local heating rate. The magenta line indicates the position of the photosphere. Regions with $Y_e \gtrsim 0.48$ and $s \lesssim 50 k_B$/baryon produce a large amount of $^{56}$Ni, which has a significant impact on the heating rate on the timescale of days.

refers to the value at 10 s for each fluid element because $^{56}$Ni is not yet fully synthesized at $r = 450$ km. In the noncollapsing models, the mass fraction of $^{56}$Ni reaches ∼10%–30% and increases with time as the neutrino-driven wind becomes more proton rich. DD2_q1.77 exhibits a comparably low mass fraction due to its long-lasting spiral-wave wind ejecta component, which ejects slightly neutron-rich matter alongside the polar proton-rich wind, thereby lowering the relative fraction of $^{56}$Ni. We also observe the beginning of a neutrino-driven wind and the production of $^{56}$Ni in SFHo_q1.0, but due to its early collapse, the overall mass is much smaller than in the noncollapsing models and therefore negligible.

Note that a neutrino-driven wind is also present in previous BNS merger simulations using the leakage scheme and "M0" neutrino absorption scheme (D. Radice et al. 2018; V. Nedora et al. 2021; L. Combi & D. M. Siegel 2023). The crucial difference is that the M1 neutrino-transport scheme leads to a more massive and more proton-rich wind. In the M0 neutrino scheme, neutrinos are only transported in a radial ray-by-ray fashion. The region with the highest neutrino emissivity, however, lies at the remnant–disk interface (i.e., off-center). Thus, the neutrino-driven wind is not as massive and is ejected closer to the equatorial plane in M0 simulations. In the M1 scheme, however, neutrinos emitted from the disk interface can move vertically, leading to a more massive neutrino-driven wind with a more polar ejection angle, as already visible in older simulations that did not prescribe radial neutrino fluxes (A. Perego et al. 2014).

Figure 2 shows the spatial distribution of the ejecta 1 day after merger for the BLh_q1.49 model. The top and bottom-left quadrants show the spatial distribution of the initial electron fraction and entropy, respectively, as extracted from the NR simulation. The tidal ejecta are located close to the equatorial plane with low electron fractions and entropies, while the shock-heated ejecta are more spread out and exhibit a large range in electron fraction and entropy. In the asymmetric models, the tidal ejecta are more massive than the shock-heated ejecta (in DD2_q1.77, the tidal ejecta contribute ∼50% of the total ejecta mass), while the shock-heated ejecta are more important in the equal-mass models.

### 3.2. Nucleosynthesis

If the initial electron fraction of the ejecta is even slightly neutron rich, the small amount of free neutrons drive the composition away from the $Z = N$ line and toward the valley of stability. To produce $^{56}$Ni, the electron fraction must therefore be fairly high ($Y_e \gtrsim 0.48$). This condition leads to a sharply bounded region where the $^{56}$Ni mass fractions lie between 1% and 30%, as visible in the top-right quadrant in Figure 2 showing the mass fraction of $^{56}$Ni after 1 day. Higher entropies ($s \gtrsim 50 k_B$) disfavor the formation of seed nuclei from $\alpha$ particles, leading to less effective production of $^{56}$Ni and a higher He mass fraction. Therefore, the $^{56}$Ni mass fraction decreases for angles close to the polar axis. The high-entropy ejecta could potentially host the neutrino p ( $\nu$p) process (J. Pruet et al. 2006; C. Frohlich et al. 2006; S. Wanajo 2006; S. Wanajo et al. 2018; N. Nishimura et al. 2019). In this case, electron-antineutrino absorption on free protons create free neutrons, which are immediately captured by proton-rich seed nuclei. This way, elements between the iron group and Ag, including light $p$-nuclei can be produced. However, our network calculations do not include neutrino capture reactions and can therefore not capture this mechanism. The impact on the $^{56}$Ni abundance and the conclusions drawn in this Letter is likely negligible.

The overall ejecta masses, the mass of ejecta hosting a strong $r$-process $M_{\rm ej}^r$ (which we approximate as the ejecta with $Y_e < 0.25$), proton-rich ejecta $M_{\rm ej}^p$ ($Y_e > 0.5$), He, and $^{56}$Ni are reported in Table 1. The mass of proton-rich ejecta exceeds $10^{-3} M_\odot$ in all noncollapsing models and is highest in BLh_q1.49. In the proton-rich ejecta, the $^{56}$Ni mass fraction is approximately ∼22%–27%. At the end of the simulations employing the DD2 EOSs, the neutrino-driven wind is still ejecting matter with a high electron fraction. The $^{56}$Ni masses reported in Table 1 as well as the results that follow from it should therefore be considered lower limits in these models.

### 3.3. Kilonova Light Curve

The lower right quadrant in Figure 2 shows the local heating rate at $t = 1$ day in the BLh_q1.49 model. There are two distinct regions visible. In the neutron-rich equatorial region, the decay of $r$-process material dominates, while the decay of $^{56}$Ni is almost exclusively responsible for the nuclear energy generation in the polar region. At 1 day (roughly when the photosphere starts to enter the bulk of the ejecta), the energy generation in the two regions is already comparable.

Figure 3 shows nuclear energy generation and luminosities for the four simulations considered in this work. Solid lines in the left panel show the mass-averaged specific energy generation $\dot{q}$ due to the decay of $^{56}$Ni and $^{56}$Co, dashed lines show the combined contribution of all other isotopes, and thin lines show the total. In BLh_q1.49 and DD2_q1.0, the energy generated by the decay of $^{56}$Ni makes up more than 50% of the total heating after 3 days and more than 75% after 10 days.

Due to the large tidal ejecta mass in DD2_q1.77, the relative contribution of $^{56}$Ni is reduced, resulting in 10 (25)% after 3 (10) days. In all three models, the decay of $^{56}$Co makes up the largest part of the total energy generated around 100 days. Since the heating rate follows the decay of two nuclei, it

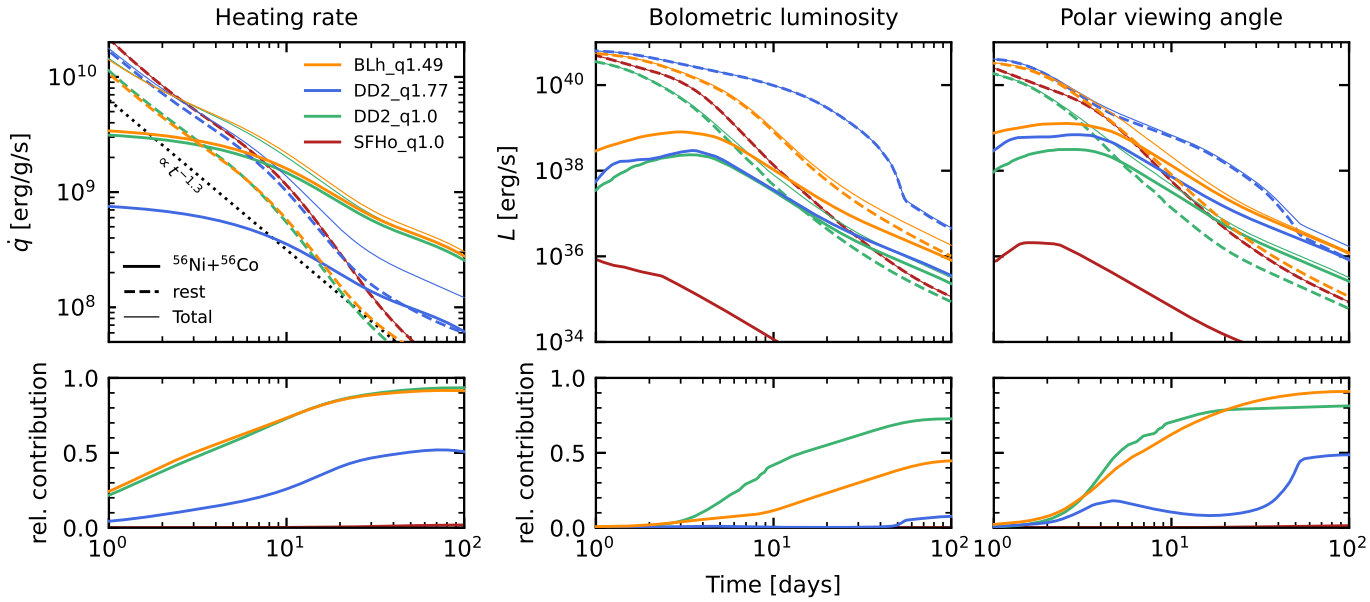



**Figure 3.** Mass-averaged nuclear energy generation (left panels), bolometric luminosity (middle panels) and luminosity observed at a viewing 20° (right panels). The upper panels show the heating and luminosities generated by the decay of $^{56}$Ni and $^{56}$Co (solid lines), the contribution of all remaining isotopes (dashed lines), and the total (thin lines). The dotted black line in the upper left panel indicates a heating rate proportional to $t^{-1.3}$. The lower panels show the relative contribution of $^{56}$Ni and $^{56}$Co in each of the above panels.

deviates significantly from the power-law behavior $\propto t^{-1.3}$ (shown as a dotted black line) expected for the combined heating of *r*-process elements. The combined heating from all other decays (dashed lines) is reasonably well described by the power law. The slight bump at a few days is caused by the $\beta$ decay of $^{132}$I, which is fed by the decay of $^{132}$Te with a half-life of 3.2 days (I. Kullmann et al. 2022).

To estimate their contribution to the light curve, we separately calculate the thermalized heating rate of $^{56}$Ni and $^{56}$Co outside the photosphere. The middle panel of Figure 3 shows the bolometric luminosity for each of the simulations (solid lines). Similar to the left panel, solid lines show the contribution from the decay chain of $^{56}$Ni outside the photosphere, and dashed lines show the difference between the total luminosity (thin lines) and the $^{56}$Ni and $^{56}$Co contribution. Within the first 5 days, the $^{56}$Ni is partially hidden within the photosphere, and its impact is thus not yet visible. Furthermore, the impact of the $^{56}$Ni heating on the bolometric light curve is smaller compared to its impact on the nuclear energy generation due to the fact that the energy of the decay is exclusively released in $\gamma$-rays and neutrinos. Since the neutrino-driven ejecta become mostly transparent to $\gamma$-rays within the first 5–10 days, the energy generated by $^{56}$Ni does not thermalize effectively. In the equatorial region, on the other hand, the $\gamma$-ray opacities are higher, and a large fraction of the energy generated by *r*-process nuclei is released by $\beta$-decay electrons, which thermalize more efficiently. While $^{56}$Co also decays primarily via electron capture, it can also decay via $\beta^+$ decay, emitting on average 121 keV via positrons per decay (M.-R. Wu et al. 2019). Therefore, after $t \gtrsim 10$ days, the impact of $^{56}$Co on the bolometric luminosity increases significantly. In `DD2_q1.77`, where the ratio of the *r*-process enriched to $^{56}$Ni enriched ejecta is very high (see $M^n_{\rm ej}$ versus $M^p_{\rm ej}$ in Table 1), the heating from $^{56}$Ni and $^{56}$Co contributes less than 10% to the total bolometric luminosity.

For a polar viewing angle, the neutrino-driven ejecta fill a large fraction of the field of view, while the tidal ejecta are subdominant. Consequently, the contribution of $^{56}$Ni and $^{56}$Co to the observed luminosities is significantly enhanced and reaches 50% after 5–7 days for `DD2_q1.0` and `BLh_q1.49`. In `DD2_q1.77`, the contribution of $^{56}$Ni and $^{56}$Co to the observed luminosity is still mostly overshadowed by the decay of *r*-process elements where the most relevant isotopes are $^{132}$I and later, the $\alpha$ emitters $^{225}$Ac, which decays with a half-life of 10 days (I. Kullmann et al. 2022) and subsequently, $^{221}$Fr. After $t \gtrsim 50$ days, their decay becomes less important, and at the same time, $\alpha$ particles begin to thermalize less efficiently than electrons and positrons. Thus, at these late times, the decay of $^{56}$Co becomes more relevant again.

We calculate the EM spectra after $t = 1$ days for `BLh_q1.49` with `TARDIS` using the ray-by-ray approach outlined above. The two most prominent features in the spectra are created by Sr and Ca (D. Watson et al. 2019; N. Domoto et al. 2021; A. Perego et al. 2022). Ca is primarily produced in the form of $^{48}$Ca in the slightly neutron-rich part of the ejecta, but ∼10% is produced as $^{40}$Ca in the proton-rich wind. Iron-group elements are not visible in the spectra due to the low luminosities at the relevant wavelengths and the dominance of Ca and Sr lines. We thus cannot identify a direct indication of proton-rich ejecta in the early spectra. While this result disfavors the emergence of an "iron-like" feature as suggested by the photometric analysis of Z.-P. Jin et al. (2016) for the afterglow of GRB 050709, it supports instead modeling efforts for the AT2017gfo spectra around the chosen epoch (see, e.g., N. Domoto et al. 2021, 2022; J. H. Gillanders et al. 2022).

The presence of *r*-process elements throughout the angle and velocity distribution of the ejecta shifts the underlying blackbody spectrum to higher wavelengths, as a result of the high line opacities of such species in the optical/UV. The latter translates in a strong line blanketing redistributing photons to lower energies, and, eventually, in a cooler blackbody due to the longer photon diffusion time (see, e.g., D. Kasen et al. 2013; M. Tanaka & K. Hotokezaka 2013).

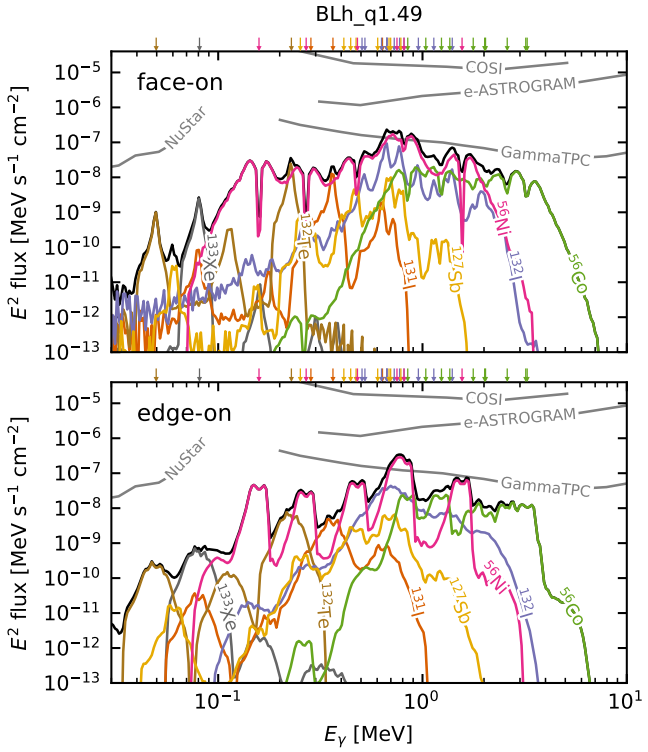



**Figure 4.** $\gamma$-ray emission spectrum at $t = 7$ days for `BLh_q1.49` at 40 Mpc for a polar (upper panel) and an equatorial (lower panel) viewing angle. Colored lines and arrows on top of the panels indicate the contribution of individual isotopes and the original line positions, respectively. Gray lines show the sensitivity of the NuStar, COSI, e-ASTROGRAM, and GammaTPC telescopes.

Note that the included line list (only Zr and lighter elements) is not sufficient to produce an accurate spectrum. However, we only perform this simple spectral modeling with a limited line list to gauge if the large abundance of Ni can produce a visible feature in the spectrum during the photospheric phase. Since we do not find any such feature, we do not pursue more realistic spectral modeling because it likely does not change the conclusion above and is outside the scope of this work.

### 3.4. Gamma-Ray Spectra

Most of the $\gamma$-rays emitted by the decay of $^{56}$Ni and $^{56}$Co escape the ejecta and thus contribute to the $\gamma$-ray spectrum. Previous works have investigated the possibility of direct detection of $\gamma$-rays from the decay of $r$-process nuclei (K. Hotokezaka et al. 2016; L.-X. Li 2019; O. Korobkin et al. 2020); however, they did not include the emission from iron-group elements. We calculate the $\gamma$-ray emission spectrum at $t = 7$ days for `BLh_q1.49` accounting for the relativistic Doppler shift for each fluid element individually.

The resulting spectrum is shown in Figure 4 for a polar (upper panel) and an equatorial viewing angle (lower panel), assuming an event distance of 40 Mpc. The partial spectra from the most relevant isotopes are shown by colored lines, and the position of the corresponding unshifted emission lines are indicated by arrows above the panels. In the energy range between 100 keV and 10 MeV, both spectra are dominated by $^{56}$Ni and $^{56}$Co lines. From a polar viewing angle, the wind ejecta are moving either away (below the merger remnant) or toward the observer (above the merger remnant). Lines from $^{56}$Ni and $^{56}$Co are thus either red- or blueshifted and form a double peak. $\gamma$-rays from $r$-process elements stem mostly from the tidal ejecta in the equatorial plane, resulting in narrower lines. For an edge-on equatorial observer, peaks from $^{56}$Ni and $^{56}$Co are instead narrower, while those from $r$-process isotopes are broader. Before $\sim$1 day, the $\gamma$-rays produced by the decay of $^{56}$Ni do not escape the ejecta, and the $^{56}$Ni peak in the spectrum is not yet visible. At $\sim$3–15 days, the $^{56}$Ni lines are the most dominant peaks in the spectrum. After $\sim$15 days, most $^{56}$Ni has decayed, and $^{56}$Co features are the most dominant.

We also include the sensitivity curve of NuStar, the Compton Spectrometer and Imager (COSI; J. A. Tomsick et al. 2023), e-ASTROGRAM (A. de Angelis et al. 2018), and GammaTPC (T. Shutt et al. 2025). Even though $\gamma$-ray emissions from $^{56}$Ni and $^{56}$Co increase the peak flux by an order of magnitude, the detection with COSI would require an event within the very optimistic distance of $\sim$5 Mpc, while e-ASTROGRAM would require $\sim$15 Mpc. However, GammaTPC would be sensitive enough to detect the double peak due to the decay of $^{56}$Ni around 700–800 keV for an event at a distance of 40 Mpc.

## 4. Discussion

We analyzed the outflow of four long-term BNS merger simulations employing an M1 neutrino-transport scheme. All noncollapsing models eject large amounts of proton-rich ejecta ($\sim 10^{-3} M_\odot$) synthesizing $\sim$4–8 $\times$ $10^{-4} M_\odot$ of $^{56}$Ni, the decay of which can significantly alter the late ($t \gtrsim 5$ day) light curve. The observation of this effect in a KN would strongly indicate that the remnant of the BNS merger did not collapse to a BH for at least $\sim$ 100 ms after the merger.

For a confirmation of our results, more work will be needed in the future. We discuss the main uncertainties in our work below.

More magnetohydrodynamics simulations including a sophisticated neutrino-transport scheme will be necessary, since magnetic fields might launch magnetically driven winds on similar timescales to the neutrino-driven wind (L. Combi & D. M. Siegel 2023; K. Kiuchi et al. 2023). This could increase the amount of polar ejecta but might reduce their electron fraction by reducing the expansion timescale of the wind ejecta and thus the total amount of neutrino captures per escaping fluid element. Note, however, that a wound-up magnetic field close to the massive NS's polar cap could trap fluid elements for longer and therefore increase the time of neutrino irradiation, similar to what is observed in magnetorotational supernova simulations (M. Obergaulinger & M.-Á. Aloy 2021). The recent work by C. Musolino et al. (2025) presents BNS merger simulations including both an M1 neutrino transport and magnetic fields. While their Figure 2 indicates the presence of some proton-rich ejecta, they do not provide quantitative information about the composition of the ejected material. The GRMHD simulations with an M1 neutrino scheme presented in A. Neuweiler et al. (2025) also show a clear enhancement in proton-rich ejecta. However, their tracer-particle scheme does not resolve this outflow, and the production of $^{56}$Ni can thus not be analyzed in detail. In preliminary MHD M1 simulation obtained with the `GR-Athena++` code (B. Daszuta et al. 2021; W. Cook et al. 2025), we find an enhancement in proton-rich ejecta if magnetic fields are included, but further analysis is needed for any definitive conclusions.

M1-type schemes are known to produce an unphysical overabundance of neutrinos in the polar regions (M. Frank et al. 2007; F. Foucart et al. 2020; D. Gizzi et al. 2021; F. Foucart et al. 2024), so one could conclude this to be responsible for the strong neutrino-driven wind in our simulations. However, D. Radice et al. (2022) found that the THC M1 neutrino transport also produces a strong proton-rich wind with the Eddington closure, which preserves the linearity of the transport operator and is therefore not affected by radiation shocks. D. Radice et al. (2022) thus conclude that the proton-rich wind is not the result of an unphysical "beam-crossing" artifact. Furthermore, F. Foucart et al. (2024) found good agreement between the M1 scheme employed in our simulations and Monte Carlo transport schemes.

The neutrino transport employed in our 3D simulations, while being state of the art for long simulations, is only approximate. Future studies with an energy-dependent neutrino-transport scheme and more accurate set of weak reactions will be needed to confirm the presence of proton-rich neutrino-driven winds from BNS merger remnants. P. C.-K. Cheong et al. (2024) perform axisymmetric MHD simulations of postmerger-like hypermassive NSs in the conformal-flatness approximation and compare energy-integrated to energy-dependent M1 neutrino schemes. They find that the energy-integrated prescription tends to overestimate the electron fraction of the ejecta within the first 50ms of postmerger evolution. However, O. Just et al. (2023) also employ an energy-dependent M1 scheme and find significant proton-rich ejecta. Future three-dimensional simulation in full GR will likely be needed to accurately gauge the impact of energy-dependent M1 schemes.

The simulations presented in this work only span $\sim$100 ms of the postmerger phase. Simulations in axisymmetry have shown that the ejection of matter might continue for seconds due to viscous heating caused by the magnetorotational instability (S. Fujibayashi et al. 2020, 2023; O. Just et al. 2023). This ejection mechanism can occur for BH and massive NS remnants and might dilute previously ejected proton-rich with slightly neutron-rich matter. In this case, the signature of the decay of $^{56}$Ni and $^{56}$Co might be hidden. However, the details of this very late phase of matter ejection are highly uncertain because second-long simulations are currently only possible with very approximate, axisymmetric viscous hydrodynamics simulation setups.

While the presence of iron-group elements has a clear impact on the nuclear energy generation, uncertainties in the thermalization efficiency complicate the quantitative characterization of the effect on the light curve. Since the thermalization efficiency of the generated energy is expected to drop rapidly on the timescale of a few days, the light curve depends sensitively on the employed thermalization treatment. This time frame overlaps with the decay time of $^{56}$Ni and $^{56}$Co, which complicates the prediction of the expected feature. The light-curve modeling employed in this work is fairly simple compared to more sophisticated radiative transport codes. The impact of $^{56}$Ni and $^{56}$Co heating on the light curve predominantly stems from a region in the ejecta that is mostly transparent on the relevant timescales of days. Thus, we expect the main source of uncertainty during the light-curve modeling to stem from the thermalization and not the radiative transport.

Note that most of these uncertainties could decrease or increase the impact of $^{56}$Ni and $^{56}$Co on the KN. Thus, we draw the following conclusion: On one hand, if a future KN observation matches the predicted signature of the decay of $^{56}$Ni and $^{56}$Co, this strongly indicates the presence of a long-lived ($\gtrsim$100 ms) merger remnant. On the other hand, if no such match is found, this could be either due to an early collapse or because proton-rich ejecta do not significantly impact the electromagnetic signal due to any of the abovementioned caveats. In this case, an interpretation requires more detailed modeling in the future to draw a definitive conclusion.

In the meantime, we suggest that future parametric studies of KNs should include the possibility for the presence of $^{56}$Ni in the ejecta. By systematically varying the abundance of $^{56}$Ni among other parameters such as ejecta mass and velocity, in a large-scale parametric study, it could be determined if the light curves of AT2017gfo and future KN observations are compatible with the presence of $^{56}$Ni independently of the simulation uncertainties mentioned above.

Furthermore, a large abundance of iron-group elements could be verified in the nebular-phase spectra. Given the strong asymmetry in the ejecta composition, the very high relative amount of $^{56}$Ni ($\sim$20%–30%) in the proton rich ejecta could lead to the presence of strong Ni and Co features on a timescale of weeks, possibly in the wavelength range $\sim$7000–7500 Å (K. Maguire et al. 2018) or in the infrared (A. Jerkstrand et al. 2025; Q. Pognan et al. 2025). However, a consistent modeling of the ionization structure would be needed in order to predict the overall and relative strengths of such features (Q. Pognan et al. 2023).

## Acknowledgments

We would like to thank David Radice for providing simulation data, James Gillanders for providing atomic data for TARDIS, and Oliver Just, Kenta Hotokezaka, and Moritz Reichert for fruitful discussions and comments. S.B. and M.J. acknowledge support by the EU Horizon under ERC Consolidator grant, No. InspiReM-101043372. F.M. acknowledges support from the Deutsche Forschungsgemeinschaft (DFG) under grant No. 406116891 within the Research Training Group RTG 2522/1. G.R. and A.A. acknowledge support from the Deutsche Forschungsgemeinschaft (DFG; German Research Foundation, Project ID 279384907, SFB 1245) and the State of Hesse within the Research Cluster ELEMENTS (Project ID 500/10.006). E.L. acknowledges support by the European Union—NextGenerationEU RFF M4C2 1.1 PRIN 2022 project 2022RJLWHN URKA. The work of AP is partially funded by the European Union—Next Generation EU, Mission 4 Component 2—CUP E53D23002090006 (PRIN 2022 Prot. No. 2022KX2Z3B). Simulations were performed on SuperMUC-NG at the Leibniz-Rechenzentrum (LRZ) Munich and on the national HPE Apollo Hawk at the High Performance Computing Center Stuttgart (HLRS). The authors acknowledge the Gauss Centre for Supercomputing e.V. (https://www.Gauss-center.eu) for funding this project by providing computing time on the GCS Supercomputer SuperMUC-NG at LRZ (allocations pn36ge, pn36jo, pn68wi, and pn76li). The authors acknowledge HLRS for funding this project by providing access to the supercomputer HPE Apollo Hawk under the grant Nos. INTRHYGUE/44215 and MAGNETIST/44288. Postprocessing and development runs were performed on the ARA cluster at Friedrich Schiller University Jena. The ARA cluster is funded in part by DFG grants INST 275/334-1 FUGG and

INST 275/363-1 FUGG, and ERC Starting Grant, grant agreement No.– BinGraSp-714626.

## ORCID iDs

Maximilian Jacobi https://orcid.org/0000-0001-8168-4579
Fabio Magistrelli https://orcid.org/0009-0005-0976-7851
Eleonora Loffredo https://orcid.org/0000-0001-7888-9733
Giacomo Ricigliano https://orcid.org/0000-0003-1626-1355
Leonardo Chiesa https://orcid.org/0000-0002-5112-1975
Sebastiano Bernuzzi https://orcid.org/0000-0002-2334-0935
Albino Perego https://orcid.org/0000-0002-0936-8237
Almudena Arcones https://orcid.org/0000-0002-6995-3032

## References

Abbott, B. P., Abbott, R., Abbott, T. D., et al. 2019, PhRvX, 9, 011001
Bernuzzi, S., Magistrelli, F., Jacobi, M., et al. 2025, MNRAS, 542, 256
Bombaci, I., & Logoteta, D. 2018, A&A, 609, A128
Cheong, P. C.-K., Foucart, F., Duez, M. D., et al. 2024, ApJ, 975, 116
Combi, L., & Siegel, D. M. 2023, ApJ, 944, 28
Cook, W., Daszuta, B., Fields, J., et al. 2025, ApJS, 277, 3
Cowperthwaite, P. S., Berger, E., Villar, V. A., et al. 2017, ApJL, 848, L17
Cyburt, R. H., Amthor, A. M., Ferguson, R., et al. 2010, ApJS, 189, 240
Daszuta, B., Zappa, F., Cook, W., et al. 2021, ApJS, 257, 25
de Angelis, A., Tatischeff, V., Grenier, I. A., et al. 2018, JHEAp, 19, 1
Dessart, L., Ott, C. D., Burrows, A., Rosswog, S., & Livne, E. 2009, ApJ, 690, 1681
Domoto, N., Tanaka, M., Kato, D., et al. 2022, ApJ, 939, 8
Domoto, N., Tanaka, M., Wanajo, S., & Kawaguchi, K. 2021, ApJ, 913, 26
Eichler, D., Livio, M., Piran, T., & Schramm, D. N. 1989, Natur, 340, 126
Foucart, F., Cheong, P. C.-K., Duez, M. D., et al. 2024, PhRvD, 110, 083028
Foucart, F., Duez, M. D., Hebert, F., et al. 2020, ApJL, 902, L27
Frank, M., Klar, A., Larsen, E. W., & Yasuda, S. 2007, JCoPh, 226, 2289
Freiburghaus, C., Rosswog, S., & Thielemann, F. K. 1999, ApJ, 525, L121
Frohlich, C., Martínez-Pinedo, G., Liebendorfer, M., et al. 2006, PhRvL, 96, 142502
Fujibayashi, S., Kiuchi, K., Wanajo, S., et al. 2023, ApJ, 942, 39
Fujibayashi, S., Wanajo, S., Kiuchi, K., et al. 2020, ApJ, 901, 122
Galeazzi, F., Kastaun, W., Rezzolla, L., & Font, J. A. 2013, PhRvD, 88, 064009
Gillanders, J. H., Smartt, S. J., Sim, S. A., Bauswein, A., & Goriely, S. 2022, MNRAS, 515, 631
Gizzi, D., Lundman, C., O'Connor, E., Rosswog, S., & Perego, A. 2021, MNRAS, 505, 2575
Goodale, T., Allen, G., Lanfermann, G., et al. 2003, in Proc. of VECPAR 2002, 2565, 197
Gutiérrez, E. M., Bhattacharya, M., Radice, D., Murase, K., & Bernuzzi, S. 2025, PhysRevD, 111, 063031
Hempel, M., & Schaffner-Bielich, J. 2010, NuPhA, 837, 210
Hotokezaka, K., Kiuchi, K., Kyutoku, K., et al. 2013, PhRvD, 88, 044026
Hotokezaka, K., Wanajo, S., Tanaka, M., et al. 2016, MNRAS, 459, 35
Jerkstrand, A., Pognan, W., Banerjee, S., et al. 2025, arXiv:2510.12410
Jin, Z.-P., Hotokezaka, K., Li, X., et al. 2016, NatCo, 7, 12898
Just, O., Vijayan, V., Xiong, Z., et al. 2023, ApJL, 951, L12
Kasen, D., Badnell, N. R., & Barnes, J. 2013, ApJ, 774, 25
Kasliwal, M. M., Nakar, E., Singer, L. P., et al. 2017, Sci, 358, 1559
Kerzendorf, W. E., & Sim, S. A. 2014, MNRAS, 440, 387
Kiuchi, K., Fujibayashi, S., Hayashi, K., et al. 2023, PhRvL, 131, 011401
Korobkin, O., Rosswog, S., Arcones, A., & Winteler, C. 2012, MNRAS, 426, 1940
Korobkin, O., Hungerford, A. M., Fryer, C. L., et al. 2020, ApJ, 889, 168
Kullmann, I., Goriely, S., Just, O., et al. 2022, MNRAS, 510, 2804
Li, L.-X. 2019, ApJ, 872, 19
Li, L.-X., & Paczynski, B. 1998, ApJL, 507, L59
Lippuner, J., & Roberts, L. F. 2015, ApJ, 815, 82
Lippuner, J., & Roberts, L. F. 2017, ApJS, 233, 18
Logoteta, D., Perego, A., & Bombaci, I. 2021, A&A, 646, A55
Magistrelli, F., Bernuzzi, S., Perego, A., Jacobi, M., & Fontes, C. J. 2025, arXiv:2512.11032
Magistrelli, F., Bernuzzi, S., Perego, A., & Radice, D. 2024, ApJL, 974, L5
Maguire, K., Sim, S. A., Shingles, L., et al. 2018, MNRAS, 477, 3567
Martin, D., Perego, A., Arcones, A., et al. 2015, ApJ, 813, 2
Metzger, B. D., Martínez-Pinedo, G., Darbha, S., et al. 2010, MNRAS, 406, 2650
Morozova, V., Piro, A. L., Renzo, M., et al. 2015, ApJ, 814, 63
Murguia-Berthier, A., Ramirez-Ruiz, E., Kilpatrick, C. D., et al. 2017, ApJL, 848, L34
Musolino, C., Rezzolla, L., & Most, E. R. 2025, ApJL, 984, L61
Nedora, V., Bernuzzi, S., Radice, D., et al. 2019, ApJL, 886, L30
Nedora, V., Bernuzzi, S., Radice, D., et al. 2021, ApJ, 906, 98
Neuweiler, A., Gieg, H., Rose, H., et al. 2025, PhRvD, 113, 043038
Nishimura, N., Rauscher, T., Hirschi, R., et al. 2019, MNRAS, 489, 1379
Obergaulinger, M., & Aloy, M.-Á. 2021, MNRAS, 503, 4942
Perego, A., Bernuzzi, S., & Radice, D. 2019, EPJA, 55, 124
Perego, A., Radice, D., & Bernuzzi, S. 2017, ApJL, 850, L37
Perego, A., Rosswog, S., Cabezón, R. M., et al. 2014, MNRAS, 443, 3134
Perego, A., Vescovi, D., Fiore, A., et al. 2022, ApJ, 925, 22
Pognan, Q., Grumer, J., Jerkstrand, A., & Wanajo, S. 2023, MNRAS, 526, 5220
Pognan, Q., Kawaguchi, K., Wanajo, S., Fujibayashi, S., & Jerkstrand, A. 2025, arXiv:2510.12413
Pruet, J., Hoffman, R. D., Woosley, S. E., Janka, H. T., & Buras, R. 2006, ApJ, 644, 1028
Radice, D. 2017, ApJL, 838, L2
Radice, D. 2020, Symm, 12, 1249
Radice, D., & Bernuzzi, S. 2023, ApJ, 959, 46
Radice, D., Bernuzzi, S., Perego, A., & Haas, R. 2022, MNRAS, 512, 1499
Radice, D., Galeazzi, F., Lippuner, J., et al. 2016, MNRAS, 460, 3255
Radice, D., Perego, A., Hotokezaka, K., et al. 2018, ApJ, 869, 130
Radice, D., & Rezzolla, L. 2012, A&A, 547, A26
Radice, D., Rezzolla, L., & Galeazzi, F. 2014a, MNRAS, 437, L46
Radice, D., Rezzolla, L., & Galeazzi, F. 2014b, CQGra, 31, 075012
Radice, D., Rezzolla, L., & Galeazzi, F. 2015, ASPC, 498, 121
Rosswog, S., Liebendoerfer, M., Thielemann, F. K., et al. 1999, A&A, 341, 499
Schianchi, F., Gieg, H., Nedora, V., et al. 2024, PhRvD, 109, 044012
Schnetter, E., Ott, C. D., Allen, G., et al. 2007, arXiv:0707.1607
Shutt, T., Trbalic, B., Charles, E., et al. 2025, arXiv:2502.14841
Sneppen, A., Damgaard, R., Watson, D., et al. 2024a, A&A, 692, A134
Sneppen, A., Just, O., Bauswein, A., et al. 2024b, arXiv:2411.03427
Steiner, A. W., Hempel, M., & Fischer, T. 2013, ApJ, 774, 17
Symbalisty, E., & Schramm, D. N. 1982, ApJL, 22, 143
Tanaka, M., & Hotokezaka, K. 2013, ApJ, 775, 113
Tanaka, M., Utsumi, Y., Mazzali, P. A., et al. 2017, PASJ, 69, 102
Tarumi, Y., Hotokezaka, K., Domoto, N., & Tanaka, M. 2023, arXiv:2302.13061
Tomsick, J. A., Boggs, S., Zoglauer, A., et al. 2023, ICRC, 38, 745
Typel, S., Ropke, G., Klahn, T., Blaschke, D., & Wolter, H. H. 2010, PhRvC, 81, 015803
Wanajo, S. 2006, ApJ, 647, 1323
Wanajo, S., Müller, B., Janka, H.-T., & Heger, A. 2018, ApJ, 852, 40
Watson, D., Hansen, C. J., Selsing, J., et al. 2019, Natur, 574, 497
Waxman, E., Ofek, E. O., Kushnir, D., & Gal-Yam, A. 2018, MNRAS, 481, 3423
Wu, M.-R., Barnes, J., Martínez-Pinedo, G., & Metzger, B. D. 2019, PhRvL, 122, 062701
Wu, Z., Ricigliano, G., Kashyap, R., Perego, A., & Radice, D. 2022, MNRAS, 512, 328